Ultra-Thin Solar Sails for Interstellar Travel

Phase I Final Report

December 1999

Dean Spieth
Dr. Robert Zubrin

Sponsored by:

NASA Institute for Advanced Concepts
www.niac.usra.edu
555-A 14th St., NW
Atlanta, GA 30318

NIAC CP 99-02
Period of Performance, June-November 1999
Distribution Unlimited; Approved for Public Release.

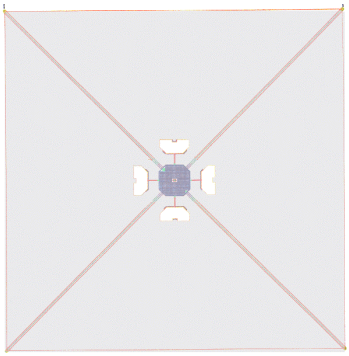

Pioneer Astronautics, Inc.
445 Union Blvd., Suite 125
Lakewood, Colorado 80228
(303) 980-0890

Table of Contents

Introduction

The solar sail is a space propulsive device, which uses a thin reflecting foil to deflect sunlight, thereby transferring the change in momentum of the solar light flux to the sail. The advantage of this concept is that it can produce thrust without the use of propellant. While accelerations are small, thrust is continuous for a long duration, enabling very high spacecraft velocities. A late 1970s artist's rendition of a solar sail intended to rendezvous with Comet Halley is shown in Figure 1. This square sail has crossed booms, reinforcing wires, stays, spars, and masts for structural support, and maneuvers by the use of vanes at the ends of the booms. An excellent summary of solar sails has recently been written in the book, *Solar Sailing* by McInnes (1999), which also discusses this solar sail.

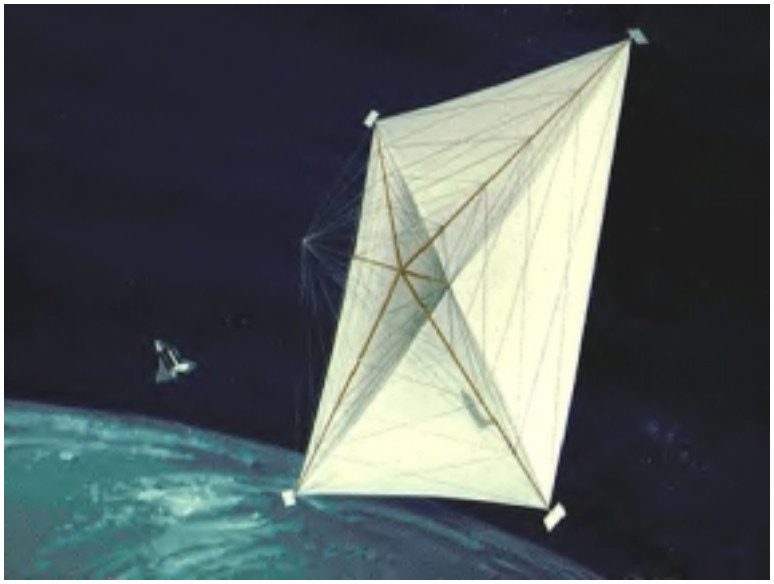

Figure 1. An Artist's Rendition of a Solar Sail (Courtesy NASA/JPL, circa 1977)

Conventional solar sails have been designed and built using thin films of aluminum approximately 100 nm thick deposited on a plastic substrate typically 5 to 25 microns thick. Aluminized Mylar or Kapton is commercially available from Sheldahl and can be used for this purpose; their 5 micron thick (0.2 mil) product is about 90% reflective and has an areal density of ~7 g/m^2. The acceleration of this material at 1 AU, excluding payload mass, will only be ~1.2 mm/s^2 limited by the mass of the plastic substrate:

$$a_c = R\, P_s/\rho_a \,, \qquad (1)$$

where the reflectivity $R = 0.9$, the solar radiation pressure $P_s = 9.12\ \mu N/m^2$, and ρ_a is the sail areal density, the sail density multiplied by the sail thickness. This acceleration is good enough to generate a spacecraft velocity increase or ΔV ~100 m/s per day at the Earth's orbit, and this sail could reach Mars within a year with a modest payload. Although this capability is of interest for inner Solar System travel, the conventional sail offers little potential for interstellar flight.

In order to overcome these acceleration limitations, Forward (1984) proposed using beamed power systems of microwaves or lasers to propel light-sail systems across interstellar space. Power requirements have been estimated at gigawatts to hundreds of terawatts, whereas we have only demonstrated several megawatts of laser power to date. Such concepts are theoretically possible and offer the potential for true relativistic interstellar flight. Landis (1998) recently revisited this concept in a NIAC Phase I study. However, the development of such high powers is well in to the future, tracking and pointing requirements become more demanding at large distances, and the system would probably require lunar deployment to avoid burning up birds, planes, and satellites if such a system were Earth based.

Metallic mesh concepts have also been developed to save sail mass, as a mesh antenna will be reflective to radio waves. If manufactured at a fine scale, such a mesh can also be manufactured today to be highly reflective to an infrared CO_2 laser and microwaves. This concept of a perforated solar sail was first suggested by Freeman Dyson in 1983 and subjected to a preliminary analysis by Robert Forward (1985). Numerous authors, including Mallove and Matloff (1989), Wright (1992), and McInnes (1999) have subsequently mentioned the idea.

An alternative to beamed power systems is to use the available sunlight and challenge the technology by producing much lighter solar sails, possibly by decreasing the plastic substrate mass or eliminating the plastic substrate altogether. It is also conceivable to perforate the remaining metallic layer to create a reflective mesh at visible wavelengths, although the required mesh line-widths are on the order of nanometers. These concepts have been considered to some extent in the literature, yet our NIAC grant, "Ultrathin Solar Sails for Interstellar Travel," is the most comprehensive evaluation of these concepts to date. If it were possible to remove the plastic substrate and retain the aluminum coating from commercially available products, the resulting sail acceleration will be over an order of magnitude higher than that of a conventional solar sail. Further orders of magnitude improvement are possible by reducing aluminum layer thickness and developing perforated sails, although manufacturing challenges are high. The following improvements in sail acceleration are possible by advanced development of manufacturing technologies:

- 25X improvement by removing the plastic substrate, leaving ~100 nm Al layer,
- 300X by reducing aluminum sail thickness to ~4 to 5 nm,
- 500-5,000X by perforating the aluminum sail, possible in the near term, and
- 10,000-100,000X by doping carbon nanotubes, well into the next century.

Physics Issues – Sail Reflectance and Acceleration

Analysis of all-aluminum solar sails resulted in predicted characteristic accelerations, a_c, of ~0.3 m/s^2 for aluminum sheets of only ~4 nm thickness, and ~0.5 to ~5 m/s^2 for aluminum grids. These accelerations are much higher than the 0.001 m/s^2 for the conventional solar sail with a plastic backing. The resolution of the large discrepancy of ~0.5 m/s^2 predicted using the theory developed by Christensen (1999), compared to the ~5 m/s^2 predicted using microwave/infrared (IR) theory, extended to visible wavelengths, is crucial at determining if a perforated sail offers vastly superior performance at solar wavelengths as suggested by physical intuition.

The reflectance and transmittance of an aluminum sheet as a function of thickness are well known and shown in Figure 2. In order to maximize the acceleration given in Equation (1) for a sheet of ultra-thin aluminum, one must trade off the increasing reflectance shown in Figure 2 in the numerator of Equation (1) with the increasing thickness in the denominator. The optimum acceleration of ~0.3 m/s^2 will then be found at ~4 nm thickness as shown in Figure 3.

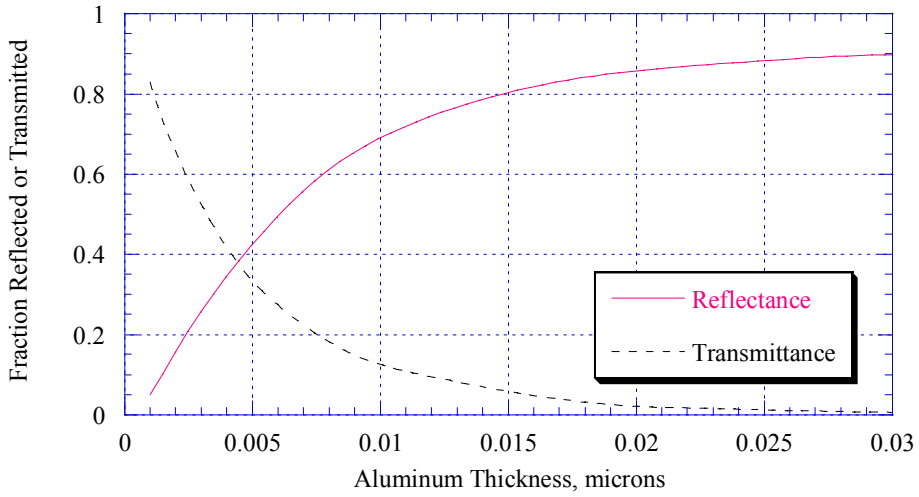

Figure 2. Predicted Solar Reflectance and Transmittance of Ultra-thin Aluminum Films

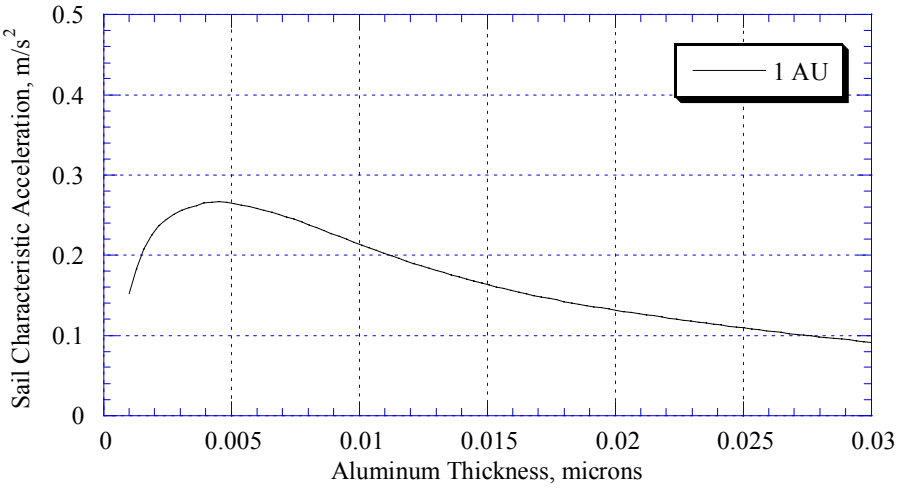

Figure 3. Predicted Self-Acceleration of an Ultra-thin Sheet of Aluminum at 1 AU

The reflectivity from a metallic grating of perfectly conducting wires is given by:

$$R = 1 - \frac{4(X_0 / Z_0)^2}{1 + 4(X_0 / Z_0)^2} \tag{2}$$

where, according to Marcuvitz (1951), for s/λ <<1,

$$\frac{X_0}{Z_0} = \frac{s}{\lambda}\left[\ln\frac{s}{2\pi r} + 0.601\left(\frac{s}{\lambda}\right)^2\right] \tag{3}$$

where s is the wire grid spacing, λ the wavelength, and r the wire radius. Figure 4 shows the reflectance of a perfectly conducting wire grid based upon Equation (2), indicating that nearly perfect reflection is obtained at the smaller wire spacing to wire radius ratio of s/r = 10. As s/r is increased to 100, the reflectance drops very quickly, but the mass of this grid is also 10 times less than for s/r = 10. If we attempt to incorporate the finite conductivity of the actual wire by multiplying the reflectance versus thickness results of Figure 2 for a sheet of aluminum times the result of Figure 4 for a grid, we obtain an estimated true grid reflectance shown in Figure 5.

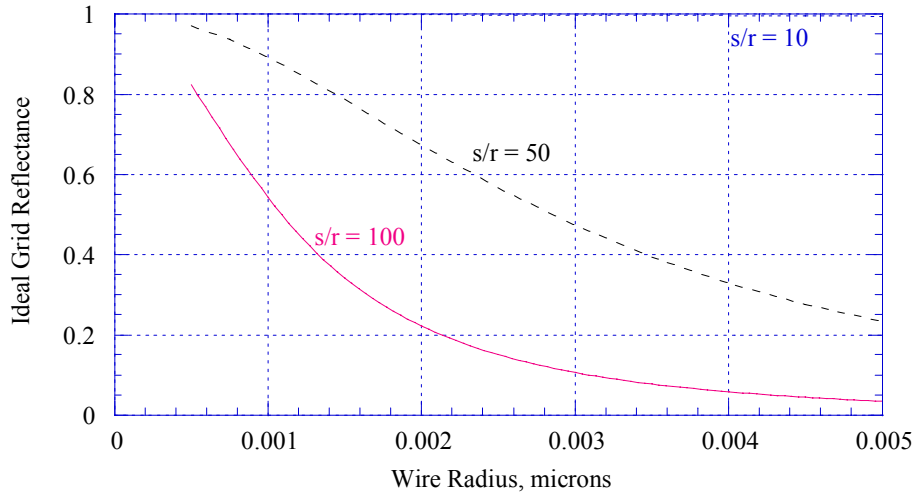

Figure 4. Predicted Reflectance of a Perfectly Conducting Nanogrid

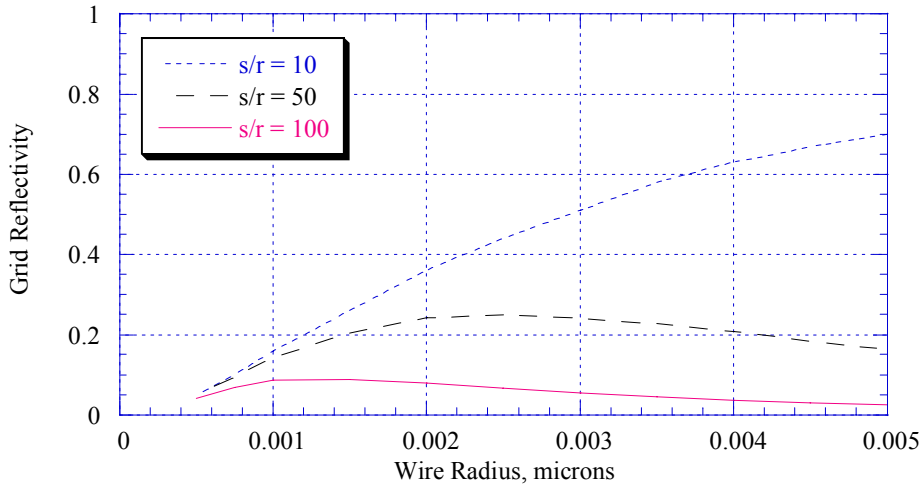

Figure 5. Predicted Reflectance of a Nanogrid, Figure 2 x Figure 4

Accounting for the mass differences of the different grid spacing, in order to predict accelerations given by Equation (1), we come up with the result that s/r = 100 should actually give the highest sail accelerations for a wire radius of approximately 1 nm, despite having the lowest reflectance. This result is shown in Figure 6. However, note that s/r = 50 which gives 80% of peak acceleration, yet with a wire radius of 1.5 nm (diameter of 3 nm) is much easier to manufacture using today's technology, and would require a sail 1/3 the area for the same net thrust. Figure 7 compares results using Marcuvitz's equations versus Forward's (1985) simplification; values are indistinguishable by s/r~10.

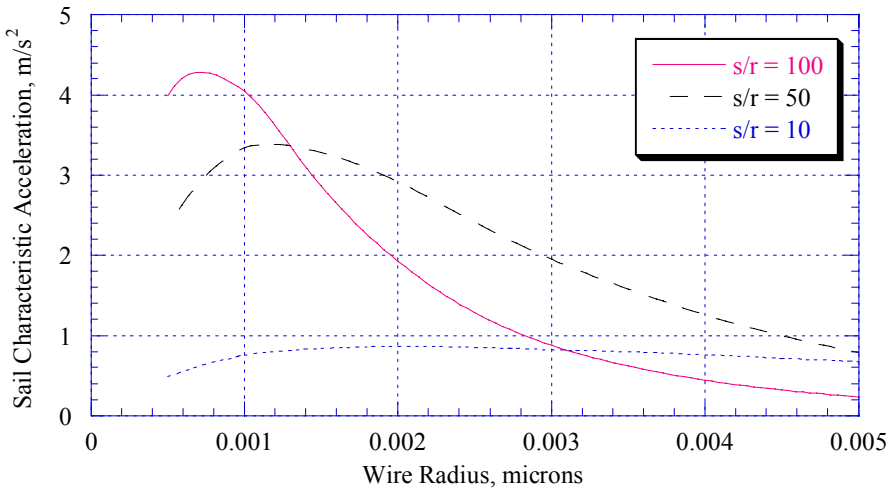

Figure 6. Predicted Acceleration of Aluminum Grid at 1 AU using Microwave Analogies

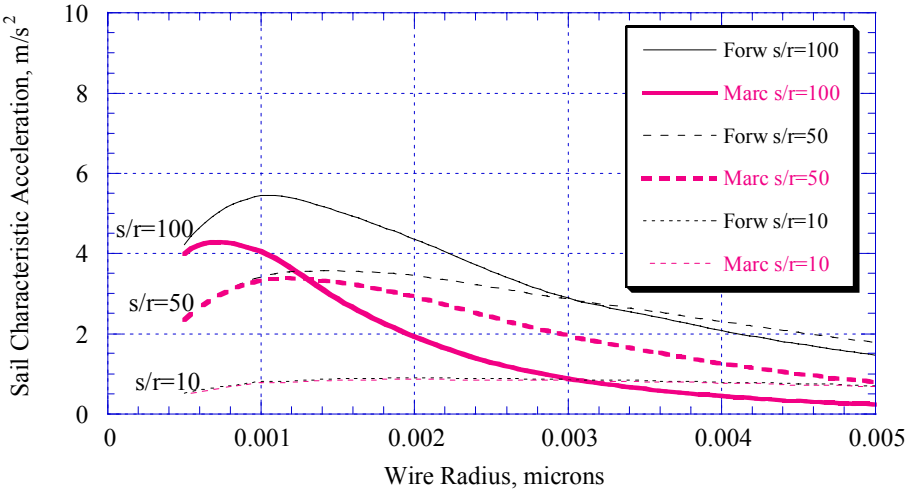

Figure 7. Predicted Accelerations Using Marcuvitz (1951) and Forward (1985) Formulas

Figure 8 is a scatter plot of accelerations predicted under this Phase I study by solving Maxwell's equations for the reflection from a grid of wires with finite electrical conductivity (Christensen, 1999). This theory is summarized in Appendix A. In this theory an optimum acceleration of ~0.5 m/s^2 is obtained at a wire radius of 5 nm and s/r = 10. This is nearly an order of magnitude less than the result obtained by extending microwave/IR theory. It is therefore crucial that this issue be explored experimentally, as these results are key as to the future of the perforated solar sail.

This theory was then applied to a sail mesh of carbon nanotubes rather than aluminum (Christensen, 1999). Carbon is less dense, the nanotubes are hollow thus saving tremendous weight, and the extended temperature capabilities of carbon should enable close approach to the sun, thus developing much higher accelerations for interstellar travel. Because carbon is not very reflective at visible wavelengths, initial predictions were not much better than those using an aluminum mesh. However, by adding a metallic coating to or doping the carbon nanotubes, the reflectivity can be greatly enhanced. Doping of carbon nanotubes has recently been demonstrated (Dekker, 1999). Characteristic accelerations of 17 m/s^2 were predicted for these doped nanotubes, and if extensions of microwave/IR theory are valid, characteristic accelerations over 100 m/s^2 may be possible using doped carbon nanotubes in the far term.

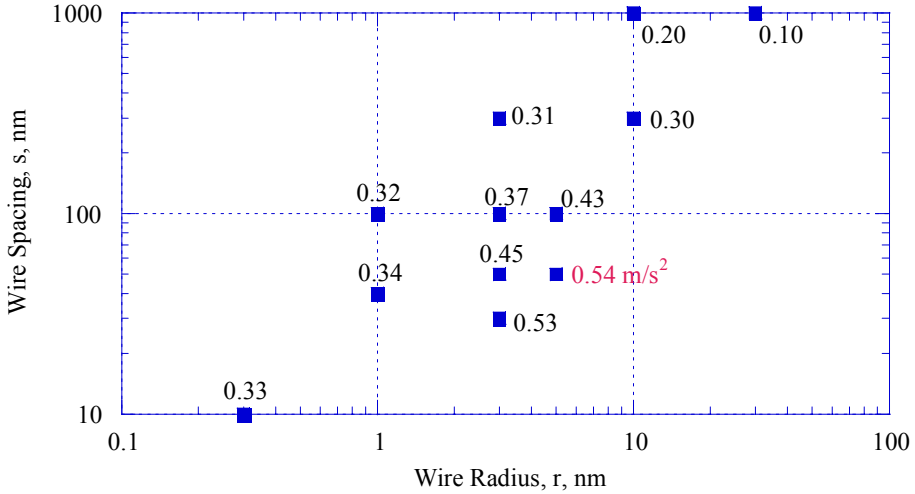

Figure 8. Scatter Plot of Characteristic Accelerations Predicted Using Resistive Theory for an Aluminum Grid at 1 AU

Thermal and Structural Engineering Considerations

A solar sail developed for interstellar travel must travel as close to the sun as possible, in order to maximize solar radiation pressure and hence sail acceleration. Sail temperature will limit closest perihelion passage. In order to predict the temperature of the solar sail as a function of solar distance, we need to predict the solar absorptance and emittance of an aluminum sail as a function of thickness. The solar absorptance is simply $\alpha_s = 1- r_s - \tau_s$, where r_s is the solar reflectivity and τ_s is the solar transmittance shown in Figure 2 as a function of thickness. The thermal emittance will simply be $\varepsilon = 1 - r_{ir} - \tau_{ir}$, where the infrared (ir) reflectance and transmittance are weighted by the Planck function at the temperature of interest. There will be a small difference between hemispherical and normal emittance that will be neglected in this analysis.

Predicted results for the solar absorptance and thermal emittance of ultra-thin sheets of aluminum are shown in Figure 9. At 30 nm thickness, we predict a solar absorptance of 0.1 and emittance of 0.03, consistent with measurements for bulk properties of aluminum. The α/ε ratio is high, which can result in high temperatures under solar illumination. However, at a few nanometers thickness, the α/ε ratio is expected to drop below one that will result in much lower solar equilibrium temperatures. The increase in solar absorptance is consistent with that presented by Forward (1984). The increase in emittance at a few nanometers thickness is consistent with increasing emittance with higher sheet resistivity, but should be experimentally verified. We have not accounted for the temperature dependence on optical properties, which should also be measured; however, based upon Figure 4, the emittance should increase slightly with temperature for thick films, and probably decrease slightly with temperature for films of only a few nanometers.

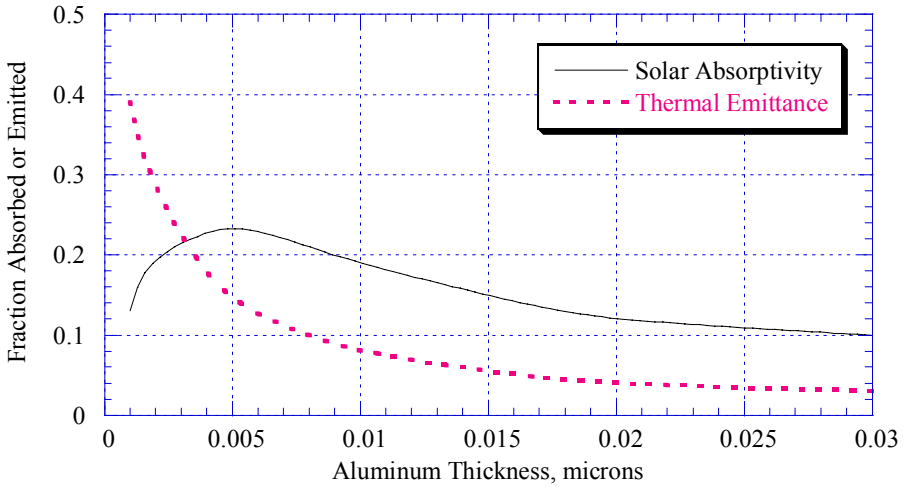

Figure 9. Predicted Solar Absorptance and Thermal Emittance for Thin Aluminum Layers

In earlier solar sail studies, a thin layer of chromium was used on the back of the plastic support membrane, with aluminum on the front; chromium has a higher resistivity than aluminum, and emittances of >0.6 (Rowe, 1978) were obtained as chromium thickness was decreased to 10 nm, similar to the trend predicted for aluminum except at larger thickness. A high emittance is desirable to minimize sail temperatures and achieve closer approaches to the sun. However, a 10

nm thick layer of chromium on a ultra-thin solar sail with only a few nanometers of aluminum would drastically increase the mass of the sail, and reduce its acceleration more so than a closer solar approach would increase its acceleration.

For an aluminum nano-grid, the solar absorptance should decrease as the cross-sectional area is reduced, and the emittance should remain the same. This should be experimentally verified. Using a wire grid should enable closer approaches to the sun and hence higher accelerations.

Based upon the predicted optical properties of Figure 9, an ultra-thin aluminum sheet of only 2 nm thickness should be able to approach within 0.2 AU of the sun, reaching a temperature of 400°C as shown in Figure 10. This is a worst case temperature at normal incidence to the sun's rays, and accounts for front and back emission. Although it might be possible to approach to 0.1 AU before the sail melts, the sail's strength will already be greatly reduced at 0.2 AU.

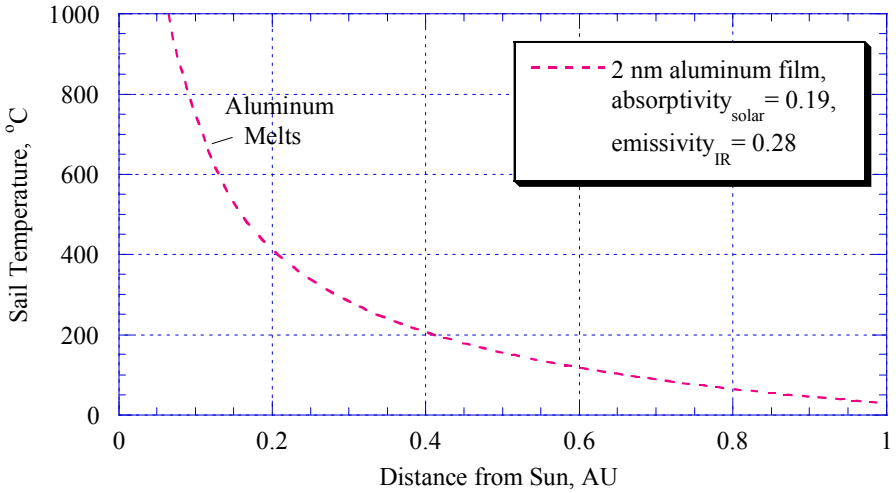

Figure 10. Predicted Temperature of an Ultra-thin Sheet of Aluminum with Solar Approach

There is a dramatic reduction in the mechanical properties of metals with temperature ; for aluminum, tensile strength is reduced to 10-20 MPa by 400°C as shown in Figure 11. Predicted sail tensile stresses are shown in Figure 12, indicating that sail radius of curvature must be less than 1 km to keep tensile stress below 10 Mpa. For extremely large solar sails, gores may have to be incorporated into sail design, similar geometrically to the surface of a pumpkin, to reduce tensile stresses. This design is already planned for future stratospheric super-pressure balloons (Smith and Cutts, 1999).

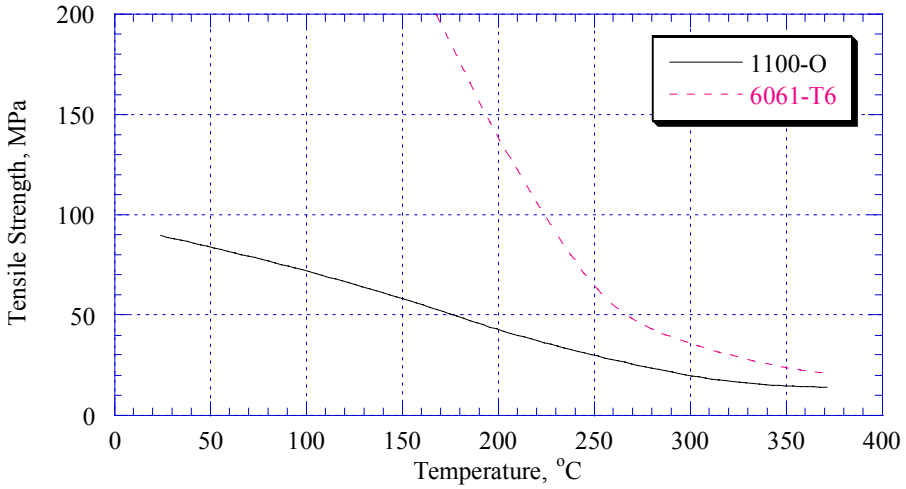

Figure 11. Tensile Strength versus Temperature for Two Alloys of Aluminum

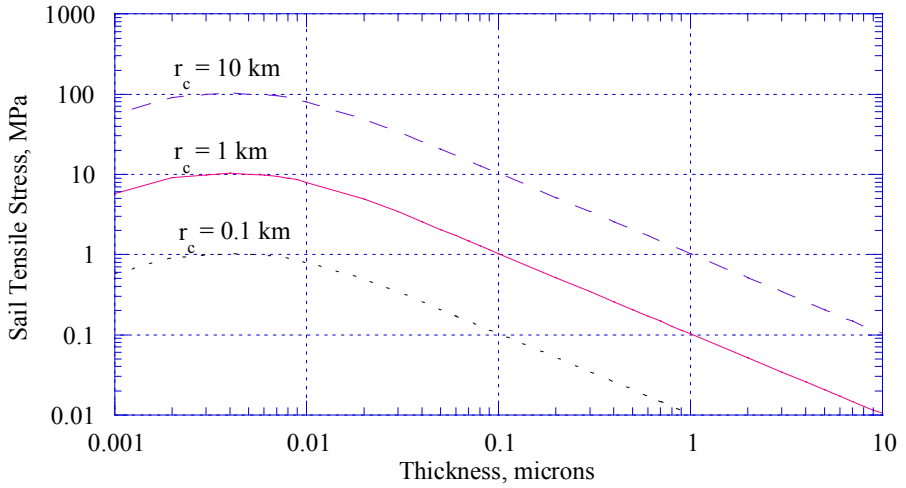

Figure 12. Tensile Stress versus Sail Thickness and Curvature at 0.2 AU

In the far-term, solar sails may eventually be constructed of carbon fibers or carbon nanotubes. Thermally, carbon-carbon can survive temperatures of ~3000°C before outgassing becomes excessive. Structurally, carbon-carbon has continuous use temperatures exceeding 1600°C; furthermore, its structural properties remain relatively constant over this range, unlike the structural properties of metals shown in Figure 11. If carbon-carbon can be doped or coated with a high temperature material to enhance its solar reflectivity, then a carbon sail can probably approach within four solar radii of the sun, enabling extremely high accelerations.

Manufacturing Issues for an Ultra-thin Solar Sail

The manufacture of a thin sheet of aluminum on plastic can be accomplished today. The aluminized Mylar and Kapton materials used for spacecraft thermal control have aluminum layers on the order of 100 nm thick. However, low emissivity window films are also mass produced with film layers as thin as 5 to 10 nm. Astronomical X-ray film layers can be as thin as 1 nm. So the production of a few nanometer film of aluminum on plastic can be produced today in large quantities.

The key challenges for the implementation of an ultra-thin solar sail sheet include removal of the plastic supporting substrate after deployment by outgassing and/or radiation degradation, adding rip-stop mesh for added strength, and attachment of support booms and payload.

Normally, thin film depositions of coatings such as aluminum are highly adherent and may include a bond layer to further enhance adhesion. In this case, we desire a strong enough bond that will survive sail deployment, but then detach with temperature or UV irradiation. A diamond-like carbon (DLC) bond layer has been reported to degrade with UV (McInnes, 1999). If a bond layer can be developed which will cleanly remove the substrate, then choice of a substrate can be based on cost considerations. Mylar, for example, is less expensive than Kapton. If one must rely on the substrate to outgas, then a lower temperature substrate such as polyethylene may be desired. This issue of gracefully removing the plastic substrate requires considerable experimentation.

Rip-stops are common in boat sails in order to prevent a crack from propagating across an entire sail. There has been some work performed at adding rip-stops into a polyimide plastic substrate by SRS Technologies in Huntsville. Their LaRC™-CP1 fluorinated polyimide product with embedded Kevlar rip-stops is shown in Figure 13; this sample is 5 microns thick although they also offer 2.5 micron thick CP1. Note there is a great deal of wrinkling which may scatter sunlight rather than reflecting it specularly for obtaining maximum solar radiation thrust. Kapton polyimide is taped around the perimeter; note that the CP1 polyimide is clear rather than gold. For ultra-thin solar sails, it will be necessary to embed rip-stops in the aluminum layer, since there will be no plastic substrate after sail deployment.

The key challenge for a nanogrid or reflective wires is its manufacture. Figure 6 shown earlier suggests an optimum sail acceleration using 1 to 3 nm radius (2 to 6 nm width) gridlines, with optimum grid spacing to grid radius ratios of 50 to 100 (i.e., spacing to gridline width ratios of 25 to 50). High resolution Scanning Electron Microscopes (SEMs) can resolve less than a nanometer, so theoretically it should be possible to manufacture a nanogrid for the dimensions of interest. In practice, SEMs have written features approaching 5 nm in an organic resist, while Scanning Transmission Electron Microscopes (STEMs) have written feature sizes smaller than 2 nm in an inorganic resist.

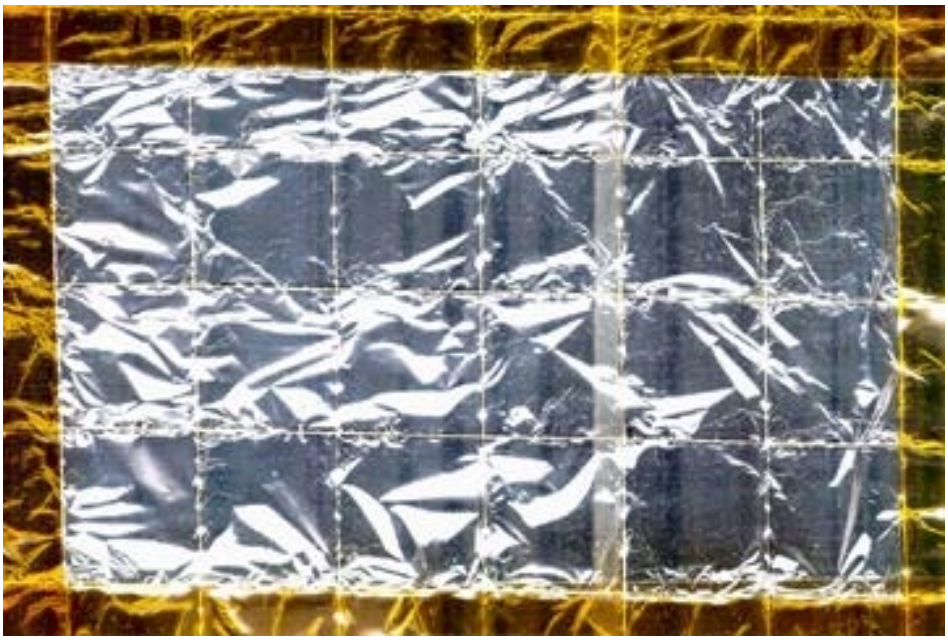

Figure 13. SRS Technologies LaRC™-CP1 Fluorinated Polyimide with Embedded Rip-Stops

Microelectronics manufacturing utilizes optical lithography and is approaching feature sizes of ~100 nm (0.1 micron technology); they have not utilized SEM technology because of the low throughput of SEMs. The use of UV lasers to drill holes on the scale of ~100nm, with precise spacing of perhaps ~102 to 110 nm, may be possible in the future with precision stage control. Forward (1990) has also suggested using two UV laser beams to create a holographic fringe pattern with a spacing of 200 nm, where line widths could be varied by changing resist exposure and development times.

Operational Issues of an Ultra-thin Solar Sail

Deployment of ultra-thin solar sails should be similar to conventional solar sails with a plastic backing, as the plastic support backing of the ultra-thin solar sail will be intact during deployment, and disintegrate after deployment due to radiation and/or thermal effects.

Deployment will become more challenging as solar sails are made larger. Figure 14 shows the payload capability of different solar sail technologies as a function of sail size. DARPA is funding a number of universities to develop nanosats weighing less than 10 kg, whereas some organizations consider nanosats as weighing less than 1 kg. An aluminized Kapton, conventional solar sail of only 40 m (0.040 km) on a side will weigh almost 10 kg, and will have an acceleration at 1 AU of 1.4 mm/s^2 if payload mass << sail mass. For a payload mass of 10 kg, the acceleration would only be reduced a factor of two. An ultrathin all-aluminum sail only 4 nm thick and 1 km on a side also weighs 10 kg, and is capable of carrying a nanosat class payload. Furthermore, it is capable of ~200X higher accelerations. A nanomesh of aluminum wires is estimated to be nearly 40 km on a side to carry a comparable payload, yet is capable of an additional order of magnitude acceleration increase, and is capable of a 10,000 AU mission within a couple decades. By the time nanogrid technology can be developed for mass production, it is more likely that spacecraft masses can be reduced below 0.1 kg by using MEMS, multifunctional structures, and further microcircuit size reductions. Sail size requirements would then reduce to 400 m for nanogrid sails and only 100 m for ultrathin sheet sails. These sail sizes are far more practical when considering the weight of the plastic backing for launch, which of course will be removed in space after sail deployment.

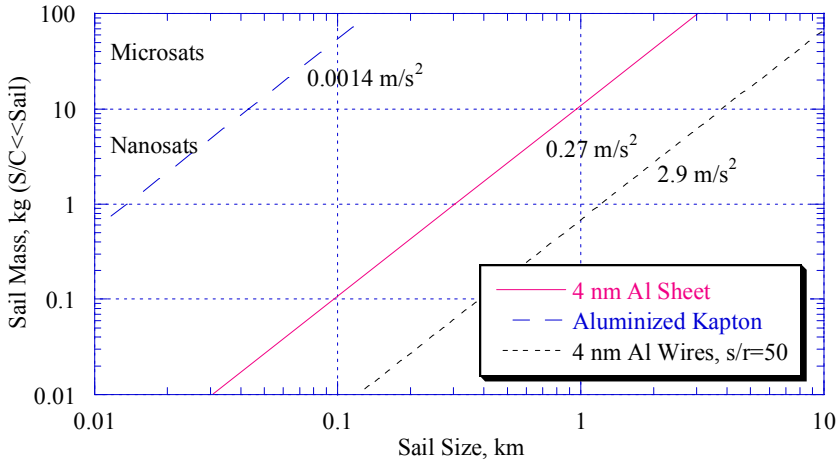

Figure 14. Solar Sail Size and Mass for Various Sail Technologies

Control of the sail should be relatively simple, as interstellar probes are likely to accelerate directly out from the sun to achieve maximum acceleration. A probe is likely to position the packaged sail at the appropriate coordinates close to the sun, at which time the sail will deploy, the plastic backing will detach, and the interstellar mission will be on its way. Only minimal control will be needed to offset unexpected disturbances. That is, steering vanes will not be needed at the end of the booms as shown earlier in Figure 1, as attitude corrections can be performed from the payload location.

Such a design is shown in Figure 15, developed by Pioneer Astronautics. There are four control vanes attached to the spacecraft, eliminating the need for vanes at the end of each boom shown in Figure 1. Computer simulations demonstrated that these centralized control vanes provided adequate control authority in Earth orbit, so they are more than adequate for interstellar missions. The spacecraft is at the center of the sail and there are no complicated guide wires to support it. Figure 16 shows a 25% scale model of a conventional solar sail built by Pioneer Astronautics for BMDO, which demonstrated an inflatable boom system utilizing UV self-curing stiffening resins. For further reductions in flight weight, after the sail is deployed the spacecraft could be rotated and then the booms could be discarded. Alternatively, designs are possible in which sail deployment could be accomplished entirely by rotational means. Initially, interstellar and deep space missions will require little control, so such simple, lightweight designs are optimal.

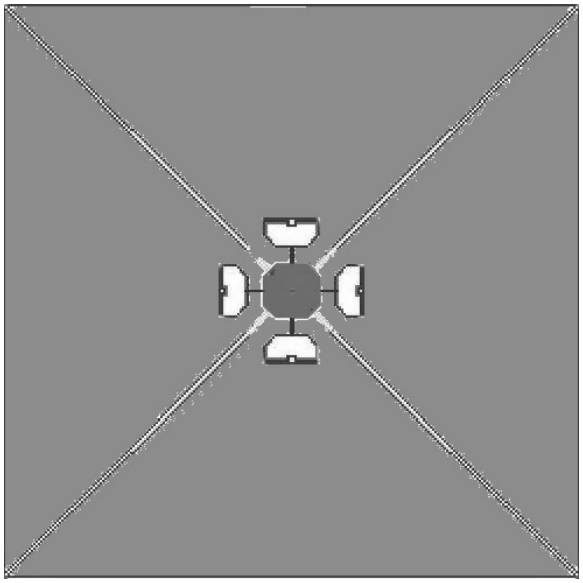

Figure 15. Pioneer Astronautics Lightweight Solar Sail using Inflatable Booms

Figure 16. A Pioneer Astronautics Inflatable Boom Solar Sail Deployed in a Hotel Ballroom

Mission Analysis for an Ultra-thin Solar Sail

Acceleration and the distance of closest solar approach are the key variables that determine if a solar sail can reach velocities of interest for interstellar travel. Usually, the characteristic acceleration, a_c, i.e., the sail self acceleration at 1 AU (the Earth's orbit), is a good means of comparing one sail design to another. If solar pressure force is integrated from closest solar approach to infinity, which is the kinetic energy ($\frac{1}{2}mv^2$) gained by the sail, the terminal velocity of a solar sail will be given by:

$$v, \text{km/s} = 548\sqrt{a_c/r_s},$$

where a_c is in m/s^2 obtained from Equation (1) and r_s is the closest solar approach in AU. Table 1 shows some the missions that can be performed for an ultra-light solar sail. An ultra-thin sheet of aluminum only a few nanometers thick can achieve a_c of ~0.3 m/s^2, could reach Pluto in ~100 days, and reach the Oort cloud at ~10,000 AU within a century. In contrast, current propulsive methods would take over a decade to reach Pluto and are totally impractical to reach interstellar space. A perforated light sail made of aluminum could reach the Oort cloud in a half century if we can achieve a_c >0.5 m/s^2, and could do so in 12 years if a_c ~5 m/s^2 can be achieved. In the far term, a sail made of doped carbon nanotubes could probably approach the sun within 4 solar radii, and if it had an a_c of 10 m/s^2, could reach α Centauri in a century. A sail made of doped carbon nanostructures could reach our nearest star in a few decades if a_c >100 m/s^2 as suggested by extensions of microwave theory.

It can thus be seen that the ultrathin solar sail holds the potential to revolutionize the prospects for interstellar travel. Uniquely, with this technology, such missions could not only become feasible, but potentially cheap, since all the motive power is provided in the form of crude sunlight – no giant lasers or other power systems are required.

Table 1. Mission Times for Interplanetary and Interstellar Travel

Acceleration @ 1 AU, m/s^2	Perihelion, AU	Terminal Velocity, km/s	Time to Pluto, days	Time to 10,000 AU, yrs	Time to α Cen, yrs
0.3	0.2	671	103	71	-
0.5	0.1	1,225	56	39	-
5.0	0.1	3,875	18	12	-
10	0.019	12,572 (4.2%c)	6	4	101
100	0.019	39,756 (13%c)	1.7	1.2	32

Table 1 assumes the payload mass is negligible compared to the sail mass. If the payload mass is equal to the sail mass, accelerations will be reduced by a factor of two and trip times increased by 1.4. If the payload mass is only 10 percent of the sail mass, there will be little reduction in predicted accelerations. Also, we have made no assumption as to the size of the sail. Indeed, a small ultra-thin solar sail will accelerate just as well as a large ultra-thin sail, provided the payload mass fraction stays the same. The payload mass is the key variable that dictates sail size. With reductions in satellite size, micro-miniaturization, and fabrication of micro electro-mechanical systems (MEMS) and multifunctional structures (MFS), made possible by the needs for micro- and nano-satellites, the fabrication of solar sails is far more viable today than it was only twenty years ago, when solar sails were last considered seriously.

Summary

Solar sails have long been theorized as capable of sailing interplanetary and interstellar space. Conventional solar sail designs use aluminized plastic support membranes to form the sail, which limit their characteristic accelerations to ~0.001 m/s^2, because the plastic dominates sail mass. Such a sail is limited to travel within our solar system for missions lasting less than 10 years. By eliminating the plastic substrate after sail deployment, it is possible to increase the sail acceleration three-hundred fold. This sail can venture anywhere in our solar system within a year. Introducing perforations in the sail, similar to an antenna mesh but at a very small nano-scale, can reduce sail mass such that accelerations of 0.5 to 5 m/s^2 are feasible. At these accelerations, a spaceship could visit the Oort cloud beyond our planetary system (~10,000 AU) within several decades. If these perforations were eventually made of carbon nano-structures rather than out of a nano-grid of aluminum, accelerations of 10 to 100 m/s^2 may be possible, enabling interstellar travel to α Centauri in less than a century. In its nearest-term and most conservative form, the utltra-thin solar sail will revolutionize outer solar system exploration. In its ultimate form, it will give humanity the stars. We therefore conclude that the development of ultra-thin solar sail technology must be aggressively pursued.

References

1. N. Marcuvitz (1951), Waveguide Handbook, McGraw-Hill, New York, p. 286.
2. W.M. Rowe, et. al. (1978), "Thermal Radiative Properties of Solar Sail Film Materials," AIAA Paper 78-852.
3. E. Drexler (1982), "Sailing on Sunlight May Give Space Travel a Second Wind," the Smithsonian, March 1982, pp. 53-60.
4. R. Forward (1984), "Roundtrip Interstellar Travel Using Laser-Pushed Lightsails," J. Spacecraft and Rockets, Vol. 21, No. 2, pp. 187-195.
5. R. Forward (1985), "Starwisp: An Ultra-Light Interstellar Probe," J. Spacecraft and Rockets, Vol. 22, No. 3, pp. 345-350.
6. E.F. Mallove and G.L. Matloff (1989), The Starflight Handbook, John Wiley, New York.
7. R. Forward (1990), "Light-Levitated Geostationary Cylindrical Orbits: Correction and Expansion," J. Astronautical Sci., Vol. 38, No. 3, pp. 335-353.
8. J.L. Wright (1992), *Space Sailing*, Gordon and Breach, Philadelphia.
9. C. Dekker (1999), "Carbon Nanotubes as Molecular Quantum Wires," Physics Today, May 1999.
10. G.A. Landis (1999), Advanced Solar and Laser Pushed Lightsail Concepts, NIAC Phase I Final Report.
11. S. Santoli (1999), "A Nanoscale Approach to Designing High Performance Bilayer Thin Films for All Metal Solar Sail Concepts," IAA-99-IAA.4.1.02, 4-8 October, Amsterdam.
12. C. Christensen (1999), Progress Report #3 for the NIAC Phase I Study, Ultra-Thin Solar Sails for Interstellar Travel.
13. I.S. Smith, Jr., and J.A. Cutts, "Floating in Space," Sci. American, Nov. 1999, pp. 98-103.
14. C.R. McInnes (1999), *Solar Sailing*, Praxis Publishing, UK.

Appendix A – Nanogrid Reflectance Equations

Dr. Cindy Christensen

The first step in calculating the reflectivity of a mesh such as that shown in Figure A1 is to analyze the electromagnetic fields impinging on an infinitely long cylindrical conductor. We follow a completely general treatment; in particular, we do *not* assume that the conductor is "good", which means we do not assume that the fields are zero inside the wire.

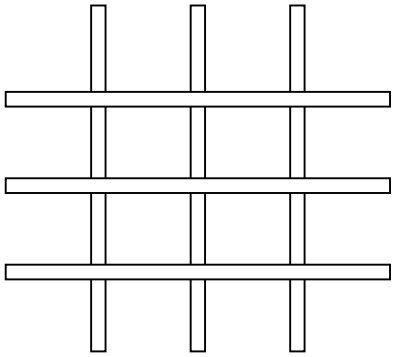

Figure A1. Mesh Geometry

In Figure A2, the cross-section is shown. The length of the wire is aligned with the z axis, coming out of the page. The incoming plane wave (1) is traveling in the +x direction and polarized in the z direction. The issue of polarization will be discussed later. Wave 2 penetrates into the conductor and wave 3 is outgoing. Both are cylindrical waves.

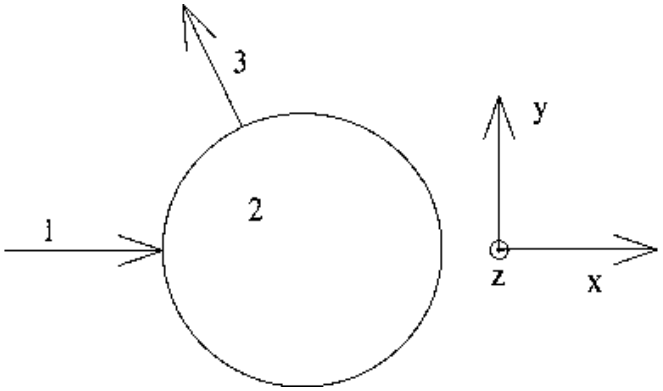

Figure A2. Cross Sectional View of a Wire

The electric field vector of wave 1 is expressed as:

$$\vec{E}_1 = E_1 \, \mathrm{Re} \exp[i(k_v x - \omega t)]$$

where k_v is the wavenumber in vacuum. For wave 2, the solutions to the Helmholtz equation in cylindrical coordinates are of the form:

$$\mathrm{Re} \, J_n(k_M r) \exp[i(n\theta - \omega t)]$$

where k_M is the wavenumber inside the medium. In general, we need to form a sum over n in order to match boundary conditions. Wave 3 is an outgoing traveling wave in cylindrical coordinates, which can be expressed as a sum of Hankel functions of the first kind:

$$H_p^{(1)}(k_v r)\exp[i(p\theta - \omega t)]$$

In order to match boundary conditions at r = a, the radius of the wire, it is desirable to express wave 1 in terms of trigonometric functions of θ. We use the Jacobi-Anger expansion:[a]

$$e^{is\cos\theta} = \sum_{m=-\infty}^{\infty} i^m J_m(s) e^{im\theta}$$

The electric fields are expressed as:

$$\vec{E}_1 = E_1 \sum_{m=-\infty}^{\infty} i^m J_m(k_v r)\, e^{i(m\theta-\omega t)}\hat{z} \qquad r > a$$
$$\vec{E}_2 = \sum_{n=-\infty}^{\infty} \tilde{E}_{n2} J_n(k_M r)\, e^{i(n\theta-\omega t)}\hat{z} \qquad r < a$$
$$\vec{E}_3 = \sum_{p=-\infty}^{\infty} \tilde{E}_{p3} H_p^{(1)}(k_v r)\, e^{i(p\theta-\omega t)}\hat{z} \qquad r > a$$

The tildes above the coefficients denote that they are complex quantities.

The B fields are obtained by Faraday's law, $\vec{\nabla}\times\vec{E} = -\frac{\partial\vec{B}}{\partial t}$:

$$\vec{B}_1 = \frac{-i}{\omega} e^{-i\omega t} \sum_{m=-\infty}^{\infty} E_1 i^m e^{im\theta}\left[\frac{im}{r} J_m(k_v r)\hat{r} - k_v J_m'(k_v r)\hat{\theta}\right]$$
$$\vec{B}_2 = \frac{-i}{\omega} e^{-i\omega t} \sum_{n=-\infty}^{\infty} \tilde{E}_{n2} e^{in\theta}\left[\frac{in}{r} J_n(k_M r)\hat{r} - k_M J_n'(k_M r)\hat{\theta}\right]$$
$$\vec{B}_3 = \frac{-i}{\omega} e^{-i\omega t} \sum_{p=-\infty}^{\infty} \tilde{E}_{p3} e^{ip\theta}\left[\frac{ip}{r} H_p^{(1)}(k_v r)\hat{r} - k_v H_p^{(1)\prime}(k_v r)\hat{\theta}\right]$$

We must match the fields inside the wire to those outside by applying boundary conditions at r = a. In this way, we can solve for the coefficients $\tilde{E}_{n2}$ and $\tilde{E}_{p3}$. However, we have not yet included all the terms. Each wire will be impinged upon by fields produced by all the other wires, so they should be included as part of the incoming wave. In general, this contribution is very difficult to deal with. We first solve the equations with these interactions neglected as an illustration.

We apply the boundary conditions at r = a:

$$E_1 + E_3 = E_2$$
$$B_{1r} + B_{3r} = B_{2r}$$
$$\frac{1}{\mu_v}(B_{1\theta} + B_{3\theta}) = \frac{1}{\mu_M} B_{2\theta}$$

[a] G. Arfken, *Mathematical Methods for Physicists*, Academic Press, Third Edition, Exercise 11.1.4

The first of these conditions give:

$$E_1 \sum_{m=-\infty}^{\infty} i^m J_m(k_v a) e^{im\theta} + \sum_{p=-\infty}^{\infty} \widetilde{E}_{p3} H_p^{(1)}(k_v a) e^{ip\theta} = \sum_{n=-\infty}^{\infty} \widetilde{E}_{n2} J_n(k_M a) e^{in\theta}$$

By orthogonality of exponentials on [0, 2π), we have:

$$E_1 i^n J_n(k_v a) + \widetilde{E}_{n3} H_n^{(1)}(k_v a) = \widetilde{E}_{n2} J_n(k_M a)$$

The second boundary condition gives the same result. The third condition yields:

$$\frac{1}{\beta}[E_1 i^n J_n'(k_v a) + \widetilde{E}_{n3} H_n^{(1)\prime}(k_v a)] = \widetilde{E}_{n2} J_n'(k_M a)$$

$$\text{where} \frac{1}{\beta} \equiv \frac{\mu_M k_v}{\mu_v k_M} = \frac{\mu_M \frac{\omega}{c}}{\mu_0 k_M} \approx \frac{\omega}{c k_M},$$

β is the complex index of refraction of the medium.

These two equations can easily be solved for $\widetilde{E}_{n3}$ and $\widetilde{E}_{n2}$. Henceforth, we shall use the notation k = k_v. When we add in the correction terms, the incoming wave receives an addition $\sum_{\substack{s=-\infty \\ s\neq 0}}^{\infty} E_3(r,\theta,s)$. Each term is the field at r and θ produced by a wire at y = sd:

$$E_1 i^n J_n(k_v a) + \sum_{\substack{s=-\infty \\ s\neq 0}}^{\infty} \sum_{j=-\infty}^{\infty} \widetilde{E}_{j3} \frac{1}{2\pi} \int_0^{2\pi} H_j^{(1)}(k_v r_s) \exp[ij(\theta_s - \tfrac{\pi}{2}) \operatorname{sgn}(s)] e^{-in\theta} \, d\theta + \widetilde{E}_{n3} H_n^{(1)}(k_v a)$$

$$= \widetilde{E}_{n2} J_n(k_M a). \qquad (1)$$

r_s and θ_s are measured from the center of the s^{th} wire. In terms of θ and r,

$$r_s = |s| d \sqrt{1 - 2\frac{r}{sd}\sin\theta + \left(\frac{r}{sd}\right)^2}$$

$$\theta_s = \sin^{-1}\left(\frac{r\cos\theta}{r_s}\right)$$

It is unfortunate that the sum over s can sometimes converge very slowly. Asymptotically, the fields go down like $r^{-1/2}$. $\sum_s \frac{1}{\sqrt{sd}}$ does not converge. The Hankel functions make this an alternating series, but they are almost periodic, and it is possible for certain wavelengths and spacings that thousands of terms may be required. The other possibility is that the terms alternate, so the sum stays near zero, and the s^{th} term does not become small compared to the sum for any small number of terms.

We must now calculate B_1. It involves the curl of the field produced by wire s ≠ 0 with respect to coordinates centered on wire s = 0. We have three boundary conditions and only two unknowns.

The system must be consistent, so we may ignore the second condition and consider only the third, which involves $B_\theta \sim -\frac{\partial E_z}{\partial r}$:

$$B_{1\theta}(\text{corr}) = \frac{-i}{\omega} e^{-i\omega t}(-)\sum_{s\neq 0}\sum_{j=-\infty}^{\infty} \tilde{E}_{j3}\left[\begin{array}{l} k_v H_j^{(1)\prime}(k_v r_s)\frac{\partial r_s}{\partial r}\exp[ip(\theta_s - \frac{\pi}{2})\text{sgn}(s)] + \\ H_j^{(1)}(k_v r_s) ip \exp[ip(\theta_s - \frac{\pi}{2})\text{sgn}(s)]\frac{\partial \theta_s}{\partial r} \end{array}\right]$$

$$\frac{\partial r_s}{\partial r} = \frac{|s| d^{\frac{1}{2}}\left(\frac{-2}{sd}\sin\theta + \frac{2r}{(sd)^2}\right)}{\sqrt{1 - 2\frac{r}{sd}\sin\theta + \left(\frac{r}{sd}\right)^2}}$$

$$\frac{\partial \theta_s}{\partial r} = \frac{\frac{\cos\theta}{r_s} - \frac{r\cos\theta}{r_s^2}\frac{\partial r_s}{\partial r}}{\pm\sqrt{1 - \left(\frac{r\cos\theta}{r_s}\right)^2}}$$

We apply $r \to a$ and insist that $a << |s|\, d$:

$$\frac{\partial r_s}{\partial r} = \frac{-sd\sin\theta}{r_s}$$

$$\frac{\partial \theta_s}{\partial r} = \frac{\cos\theta}{r_s}$$

We apply $\frac{1}{2\pi}\int_0^{2\pi} d\theta\, e^{-in\theta}$ to obtain :

$$\frac{1}{\beta}\left\{\begin{array}{l} E_1 i^n J_n'(k_v a) + \tilde{E}_{n3} H_n^{(1)\prime}(k_v a) + \\ \sum_{\substack{s=-\infty \\ s\neq 0}}^{\infty}\sum_{j=-\infty}^{\infty} \tilde{E}_{j3}\frac{1}{2\pi}\int_0^{2\pi}\left[\begin{array}{l} H_j^{(1)\prime}(k_v r_s)\left(\frac{-sd\sin\theta}{r_s}\right) + \\ H_j^{(1)}(k_v r_s)\frac{ip}{k_v}\frac{\cos\theta}{r_s} \end{array}\right]\exp\left[ip\left(\theta_s - \frac{\pi}{2}\right)\text{sgn}(s)\right]e^{-in\theta}d\theta \end{array}\right\} \quad (2)$$

$$= \tilde{E}_{n2} J_n'(k_M a)$$

Equations (1) and (2) are not immediately solvable. However, we know from experience that n = 0, ±2 are the only indices that have non-negligible coefficients. We calculate $\tilde{E}_{n3}$ for n from –5 to 5 for good measure. $E_{\pm 5}$ are typically less than 10^{-12} times E_0. We eliminate $\tilde{E}_{n2}$ between the two equations, and we have an 11×11 matrix equation, which is solved for $\{\tilde{E}_{p3}\}$. We have obtained the coefficients by considering the effects of superposition at the boundaries of the wires. We now consider the effects of superposition for all r and θ.

We have N wires, arrayed along the y axis with spacing d, each lying along the z axis. Because the grid is square, the length of each wire is Nd, where d might be of the order of 10^{-6} and N could be of order 10^{8}. As before, a is the radius.

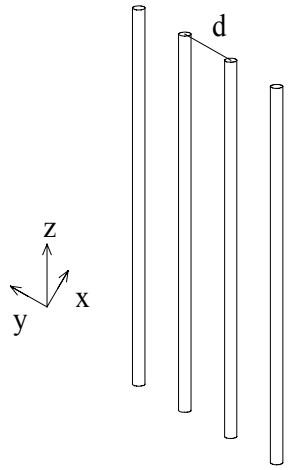

Figure A3. An Array of Wires

Because the length is so much greater than the interwire spacing, we are concerned about interference effects only in the x-y plane.

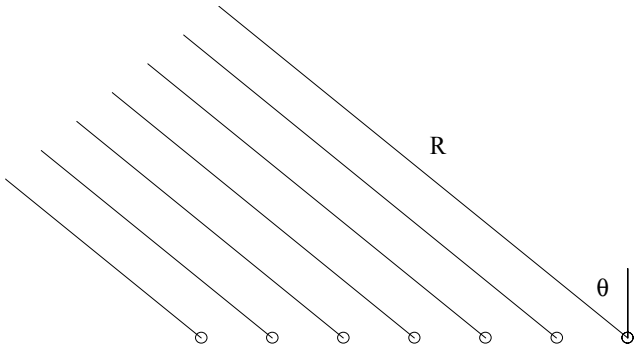

Figure A4. Geometry for Interference Effects

The treatment of this problem is very similar to that of parallel slits, which is standard in optics textbooks.[b] The derivation is given here using the particulars of this problem for the sake of completeness.

We are observing at an angle θ and a distance R from the first wire of the array. Here R >> Nd >> λ, so we are justified in using the asymptotic expansion of the Hankel functions.[c]

$$H_{\nu}^{(1)}(z) = \sqrt{\tfrac{2}{\pi z}}\exp[i(z - (\nu + \tfrac{1}{2})\tfrac{\pi}{2})]$$

[b] see, for example, E. Hecht, *Optics*, Addison-Wesley, second edition, section 10.2.3.
[c] G. Arfken, *opere citato*, Eq. 11.131

The distance from the q^{th} wire to the observer is:

$r = R - q\,d\sin\theta,$

so the total electric field is $\vec{E}_R = \sum_{q=0}^{N-1}\sum_{p=-\infty}^{\infty}\tilde{E}_{p3}\sqrt{\frac{2}{\pi kr}}\,e^{ikr}\exp[-i(p+\frac{1}{2})\frac{\pi}{2}]e^{i(p\theta-\omega t)}\,\hat{z}$
We can ignore the difference between r and R in the $r^{-1/2}$ term, which is insensitive to this variation in comparison to e^{ikr}.

$$\vec{E}_R = \hat{z}\sqrt{\tfrac{2}{\pi kR}}\sum_{p=-\infty}^{\infty}\tilde{E}_{p3}\exp[-i(p+\tfrac{1}{2})\tfrac{\pi}{2}]e^{i(p\theta-\omega t)}\sum_{q=0}^{N-1}e^{ik(R-qd\sin\theta)}$$

The sum over q equals:

$$\frac{e^{ikR}(1-e^{-ikd\sin\theta\,N})}{1-e^{-ikd\sin\theta}}$$
$$= e^{ikR}e^{-ikd\sin\theta(N-1)/2}\,\frac{(e^{i(Nkd\sin\theta)/2}-e^{-i(Nkd\sin\theta)/2})}{e^{i(kd\sin\theta)/2}-e^{-i(kd\sin\theta)/2}}$$
$$= e^{ikR-ikd\sin\theta(N-1)/2}\,\frac{\sin N\alpha}{\sin\alpha}\;\; where\;\alpha=\frac{kd\sin\theta}{2}$$

R - (N-1)/2 d sinθ is the distance from the observer to the center of the array. It should cause no confusion if we rename it r. Also,

$$\vec{E}_R = \hat{z}\sqrt{\frac{2}{\pi kr}}\,\frac{\sin N\alpha}{\sin\alpha}\sum_{p=-\infty}^{\infty}\tilde{E}_{p3}e^{ikr}\exp[-i(p+\tfrac{1}{2})\tfrac{\pi}{2}]e^{i(p\theta-\omega t)}$$
$$\vec{B}_R = \frac{-i}{\omega}\vec{\nabla}\times\vec{E}_R =$$
$$\frac{-i}{\omega}e^{-i\omega t}\left\{\begin{array}{l}\hat{r}\left[\dfrac{1}{r}\sqrt{\dfrac{2}{\pi\ k\ r}}\displaystyle\sum_{p=-\infty}^{\infty}\tilde{E}_{p3}e^{ikr}\exp[-i(p+\tfrac{1}{2})\tfrac{\pi}{2}]\left(e^{ip\theta}\,\dfrac{\partial}{\partial\theta}\,\dfrac{\sin N\alpha}{\sin\alpha}+ipe^{ip\theta}\,\dfrac{\sin N\alpha}{\sin\alpha}\right)\right]\\ -\hat{\theta}\left[\dfrac{\sin N\alpha}{\sin\alpha}\displaystyle\sum_{p=-\infty}^{\infty}\tilde{E}_{p3}\exp[-i(p+\tfrac{1}{2})\tfrac{\pi}{2}]e^{ip\theta}\sqrt{\dfrac{2}{\pi\ k\ r}}e^{ikr}\left(ik-\dfrac{1}{2r}\right)\right]\end{array}\right\}$$

from Faraday's law.

Of the two terms multiplying $\hat{r}$, both fall off with distance like $r^{-3/2}$. Of the two terms multiplying $\hat{\theta}$, one falls off like $r^{-1/2}$ and the other like $r^{-3/2}$. The terms showing $r^{-3/2}$ dependence are part of the near field and do not contribute to the traveling wave. Then $\vec{B}_R = -\frac{1}{c}E_R\hat{\theta}$, as expected.

This array of wires is most effective at reflecting waves whose electric vector is polarized parallel to the length of the wires. This polarization contains only half the power of the incident sunlight. Using a 2-D grid and taking into account the fact that sunlight is unpolarized gives the

same answers as using a 1-D grid and pretending that sunlight is polarized parallel to the wires, provided that we remember that the final sail will be approximately twice as heavy as the 1-D version. The final answer obtained in this manner will be an underestimate of the true reflectivity, because wires *will* reflect light polarized perpendicular to their length to some extent, but this is ignored by the present treatment.

To calculate the momentum transferred to the sail, we use the Maxwell stress tensor:

$$T_{ij} = \varepsilon_0(E_iE_j - \tfrac{1}{2}\,\delta_{ij}E^2) + 1/\mu_0\,(B_iB_j - \tfrac{1}{2}\,\delta_{ij}B^2)$$

A fundamental theorem of electrodynamics[d] states:

$$\vec{\nabla}\cdot(-\vec{\vec{T}}) = -\tfrac{\partial}{\partial t}\,p_M - \tfrac{\partial}{\partial t}(\mu_0\varepsilon_0\vec{S})$$

where $\vec{\vec{T}}$ is the Maxwell stress tensor and $-\vec{\vec{T}}$ is the momentum flux density in kg – m/sec per area per time. p_M is the momentum density of the matter.

$\vec{S}$ is the Poynting vector, $\frac{1}{\mu_0}\vec{E}\times\vec{B}$, so $\frac{1}{c}\vec{S}$ is the energy density of the fields and $\mu_0\varepsilon_0\vec{S} = \vec{S}/c^2$ is the momentum density.

Application of the divergence theorem in a closed volume gives the quantity of interest to us: the force on the matter present:

$$\frac{d\vec{p}}{dt} = -\varepsilon_0\mu_0\,\frac{d}{dt}\int_V \vec{S}\,d^3x + \int_S \vec{\vec{T}}\cdot d\bar{a}$$

We shall eventually average over time to remove the $e^{-i\omega t}$ factor. This is the only time dependence, i.e., the fields are stationary. Then $\int_V \vec{S}\,d^3x$ does not change in time, and the momentum imparted to the sail is given by the momentum flow across the boundary of our closed volume.

Choose a cube of edge length $\ell = Nd + \varepsilon$. We show a view from the top in Figure A5.

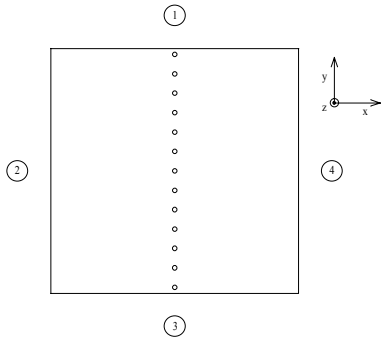

Figure A5. A Cube Control Volume Containing the Wires

[d] A good treatment is given in D. J. Griffiths, *Introduction to Electrodynamics*, Prentice-Hall, section 7.5.3

We are now dealing with quantities quadratic in field amplitudes. Re (ab) ≠ Re (a) Re (b), so we must drop the complex notation before we multiply.

$$\vec{E}_1 = E_1 \cos(kx - \omega t)\,\hat{z}$$

$$\vec{B}_1 = -\frac{E_1}{c}\cos(kx - \omega t)\,\hat{y}$$

$$\vec{E}_R = \sqrt{\frac{2}{\pi\ k\ r}}\frac{\sin N\alpha}{\sin\alpha}\sum_{p=-\infty}^{\infty} [\mathrm{Re}\,\tilde{E}_{p3}\cos(kr - p\tfrac{\pi}{2} - \tfrac{\pi}{4} + p\theta - \omega t) - \mathrm{Im}\,\tilde{E}_{p3}\sin(kr - p\tfrac{\pi}{2} - \tfrac{\pi}{4} + p\theta - \omega t)]\hat{z}$$

$$\vec{B}_R = -\tfrac{1}{c}E_R(-\sin\theta\hat{x} + \cos\theta\hat{y})$$

$$\vec{\vec{T}} = \begin{pmatrix} \frac{\varepsilon_0}{2}(E_x^2 - E_y^2 - E_z^2) + \frac{1}{2\mu_0}(B_x^2 - B_y^2 - B_z^2) & \varepsilon_0 E_x E_y + \frac{1}{\mu_0}B_x B_y & \varepsilon_0 E_x E_z + \frac{1}{\mu_0}B_x B_z \\ \varepsilon_0 E_y E_x + \frac{1}{\mu_0}B_y B_x & \frac{\varepsilon_0}{2}(E_y^2 - E_x^2 - E_z^2) + \frac{1}{2\mu_0}(B_y^2 - B_x^2 - B_z^2) & \varepsilon_0 E_y E_z + \frac{1}{\mu_0}B_y B_z \\ \varepsilon_0 E_z E_x + \frac{1}{\mu_0}B_z B_x & \varepsilon_0 E_z E_y + \frac{1}{\mu_0}B_z B_y & \frac{\varepsilon_0}{2}(E_z^2 - E_x^2 - E_y^2) + \frac{1}{2\mu_0}(B_z^2 - B_x^2 - B_y^2) \end{pmatrix}$$

$$T_{xx} = -\frac{\varepsilon_0}{2}(E_1 + E_R)^2 + \frac{1}{2\mu_0}\left[\left(\frac{E_R}{c}\sin\theta\right)^2 - \left(-\frac{E_1}{c} - \frac{E_R}{c}\cos\theta\right)^2\right]$$

$$= -\varepsilon_0[E_1^2 + E_R^2\cos^2\theta + E_1E_R(1+\cos\theta)]$$

$$T_{yx} = T_{xy} = -\varepsilon_0(E_1 + E_R\cos\theta)E_R\sin\theta$$

$$T_{zx} = T_{xz} = 0$$

$$T_{yy} = \varepsilon_0[E_1E_R(\cos\theta - 1) - E_R\sin^2\theta]$$

$$T_{zy} = T_{yz} = 0$$

$$T_{zz} = \varepsilon_0E_1E_R(1 - \cos\theta)$$

We would expect that the total momentum transfer in the y direction would be zero by symmetry. We calculate it as a check.

$$side1, d\vec{a} = (0,1,0)^T\,\ell dx$$

$$side2, d\vec{a} = (-1,0,0)^T\,\ell dy$$

$$side3, d\vec{a} = (0,-1,0)^T\,\ell dx$$

$$side4, d\vec{a} = (1,0,0)^T\,\ell dy$$

$$\text{so}\ \frac{dp_y}{dt} = \int_{-\ell/2}^{\ell/2} \varepsilon_0 [E_1(x, \tfrac{\ell}{2}) E_R(x, \tfrac{\ell}{2})(\cos\theta(x, \tfrac{\ell}{2}) - 1) - E_R{}^2 \sin^2\theta]\,\ell dx \quad ①$$

$$-\int_{-\ell/2}^{\ell/2} -\varepsilon_0 (E_1(-\tfrac{\ell}{2}, y) + E_R(-\tfrac{\ell}{2}, y)\cos\theta(-\tfrac{\ell}{2}, y)) E_R \sin\theta\,\ell dy \quad ②$$

$$-\int_{-\ell/2}^{\ell/2} \varepsilon_0 [E_1(x, -\tfrac{\ell}{2}) E_R(x, -\tfrac{\ell}{2})(\cos\theta(x, -\tfrac{\ell}{2}) - 1) - E_R{}^2 \sin^2\theta]\,\ell dx \quad ③$$

$$+\int_{-\ell/2}^{\ell/2} -\varepsilon_0 (E_1(\tfrac{\ell}{2}, y) + E_R(\tfrac{\ell}{2}, y)\cos\theta(\tfrac{\ell}{2}, y)) E_R \sin\theta\,\ell dy \quad ④$$

Consider the integrals along faces 1 and 3.

$E_1(x, \ell/2) = E_1(x, -\ell/2)$ $\qquad$ $r(x, \ell/2) = r(x, -\ell/2)$

$\sin\theta(x, \ell/2) = -\sin\theta(x, -\ell/2)$

$\cos\theta(x, \ell/2) = \cos\theta(x, -\ell/2)$

E_R is a little more difficult. $\widetilde{E}_{p3} = (-1)^p \widetilde{E}_{-p3}$. (The reader will be spared the details of the proof.) Then for $p \to -p$ and $\theta \to -\theta$,

$$\text{Re}\,\widetilde{E}_{-p3} \cos(kr + p\tfrac{\pi}{2} - \tfrac{\pi}{4} + p\theta - \omega t) = (-1)^p\,\text{Re}\,\widetilde{E}_{p3}(-1)^p \cos(kr - p\tfrac{\pi}{2} - \tfrac{\pi}{4} + p\theta - \omega t)$$

$$\text{Im}\,\widetilde{E}_{-p3} \sin(kr + p\tfrac{\pi}{2} - \tfrac{\pi}{4} + p\theta - \omega t) = (-1)^p\,\text{Im}\,\widetilde{E}_{p3}(-1)^p \sin(kr - p\tfrac{\pi}{2} - \tfrac{\pi}{4} + p\theta - \omega t)$$

The sum over p goes from $-\infty$ to ∞, so E_R is unchanged under $\theta \to -\theta$. Then the integrands of terms 1 and 3 are equal for any x, but $d\bar{a}$ points in opposite directions, so the two integrals cancel.Consider term 2. $\theta(\ell/2, y) = -\theta(\ell/2, -y)$, so again,

$E_R(\ell/2, y) = E_R(\ell/2, -y)$

$\cos\theta = \cos(-\theta)$

$\sin\theta = -\sin(-\theta)$ and E_1 is independent of y.

This means that along face 2, every point for $y > 0$ is canceled by a point $-y < 0$, and this term is zero. Term 4 meets the same fate. y momentum transfer along the faces $z = -\ell/2$ and $z = \ell/2$ are identically zero ($T_{zy} = 0$). Then there is no y momentum transfer, as we would have predicted by symmetry. z momentum transfer along faces 1, 2, 3, and 4 is zero because $T_{zx} = T_{zy} = 0$. Along the top and bottom of our box,

$$\frac{dp_z}{dt} = \int_{-\ell/2}^{\ell/2}\int_{-\ell/2}^{\ell/2} \varepsilon_0 E_1(x, y, \tfrac{-\ell}{2})\, E_R(x, y, \tfrac{-\ell}{2})(1 - \cos\theta(x, y, \tfrac{-\ell}{2}))\,dx\,dy$$

$$- \int_{-\ell/2}^{\ell/2}\int_{-\ell/2}^{\ell/2} \varepsilon_0 E_1(x, y, \tfrac{\ell}{2})\, E_R(x, y, \tfrac{\ell}{2})(1 - \cos\theta(x, y, \tfrac{\ell}{2}))\,dx\,dy$$

All terms in the integrand are independent of z, so these terms cancel, and there is no z momentum transfer, as expected. We could have invoked symmetry, but the demonstration gives us some faith in our formalism.

Any volume not containing the sail will have zero net electromagnetic momentum traveling across its closed boundary, so we can change our volume at will (as long as the new volume still contains the entire sail) and our previous results on dp_y / dt and dp_z / dt carry across.

It is found that a right circular cylinder with radius R > Nd >>1/k and height ℓ = Nd is more convenient in computing dp_x / dt.

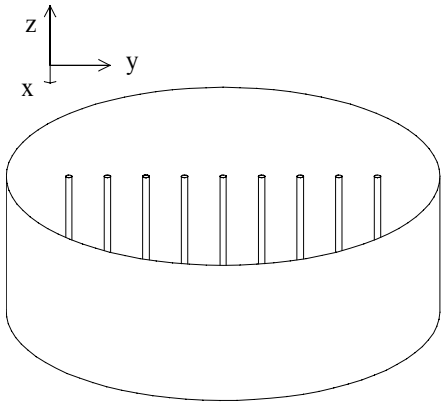

Figure A6. An Array of Wires in a Cylindrical Coordinate System

$T_{xz} = 0$, so there is no x momentum flowing across the top and bottom surfaces. Around the sides, $d\vec{a} = \ell R\, d\theta(\cos\theta\,\hat{x} + \sin\theta\,\hat{y})$. We can integrate $\vec{\bar{T}} \cdot d\vec{A}$ with respect to θ and assign the entire result to dp_x / dt, because we already know $dp_y / dt = 0$ across any closed surface containing the sail:

$$\frac{dp_x}{dt} = \ell R \int_{-\pi}^{\pi} \{-\varepsilon_0 \cos\theta [E_1^{\,2} + E_R^{\,2} \cos^2\theta + E_1 E_R (1 + \cos\theta)] - \varepsilon_0 \sin\theta (E_1 + E_R \cos\theta) E_R \sin\theta\} d\theta$$

$$= -\varepsilon_0 \ell R \int_{-\pi}^{\pi} E_1^{\,2} \cos\theta + E_R^{\,2} \cos\theta + E_1 E_R \cos\theta + E_1 E_R \, d\theta$$

In order to average over time, we will need the following identities. ωT = 2π.

$$\tfrac{1}{T}\int_0^T \cos^2(\alpha - \omega t)dt = \tfrac{1}{T}\int_0^T \sin^2(\alpha - \omega t)dt = \tfrac{1}{2}$$

$$\tfrac{1}{T}\int_0^T \cos(\alpha - \omega t)\cos(\beta - \omega t)dt = \tfrac{1}{2}\cos(\alpha - \beta)$$

$$\tfrac{1}{T}\int_0^T \cos(\alpha - \omega t)\sin(\beta - \omega t)dt = \tfrac{1}{2}\sin(\beta - \alpha)$$

$$\tfrac{1}{T}\int_0^T \sin(\alpha - \omega t)\sin(\beta - \omega t)dt = \tfrac{1}{2}\cos(\alpha - \beta)$$

The time average of the first term is:

$$\int_{-\pi}^{\pi} \tfrac{1}{T}\int_0^T E_1^{\,2} \cos^2(kR\cos\theta - \omega t)\, dt \cos\theta\, d\theta = \tfrac{E_1^{\,2}}{2}\int_{-\pi}^{\pi} \cos\theta d\theta = 0\,.$$

We have shown that $E_R(\theta) = E_R(-\theta)$. $E_1(\theta) = E_1(-\theta)$ and $\cos\theta = \cos(-\theta)$, so the integrand is an even function, and

$$\frac{dp_x}{dt} = -\varepsilon_0 \ell R 2 \int_0^\pi E_R{}^2 \cos\theta + E_1 E_R (1+\cos\theta)\, d\theta$$

○ 1 ○ 2

We treat term 2 first. This term represents the interference between the incoming and outgoing waves. We shall find it convenient to do the θ integration before summing over the N wires. This means the sin Nα / sin α term has not yet appeared. First we time average. For one wire we have:

$$\frac{1}{T}\int_0^T\int_0^\pi E_1 \cos(kx-\omega t)\sqrt{\frac{2}{\pi kr}}\sum_{p=-\infty}^{\infty}\left[\begin{array}{l}\mathrm{Re}\,\tilde{E}_{p3}\cos\left(kr - p\frac{\pi}{2} - \frac{\pi}{4} + p\theta - \omega t\right)\\ -\mathrm{Im}\,\tilde{E}_{p3}\sin\left(kr - p\frac{\pi}{2} - \frac{\pi}{4} + p\theta - \omega t\right)\end{array}\right](1+\cos\theta)\, d\theta\, dt$$

$$= \sqrt{\frac{2}{\pi kr}} E_1 \sum_{p=-\infty}^{\infty}\int_0^\pi \frac{1}{2}\left[\begin{array}{l}\mathrm{Re}\,\tilde{E}_{p3}\cos\left(kr - p\frac{\pi}{2} - \frac{\pi}{4} + p\theta - kr\cos\theta\right)\\ -\mathrm{Im}\,\tilde{E}_{p3}\sin\left(kr - p\frac{\pi}{2} - \frac{\pi}{4} + p\theta - kr\cos\theta\right)\end{array}\right](1+\cos\theta)\, d\theta$$

$$= \frac{E_1}{2}\sqrt{\frac{2}{\pi kr}}\,\mathrm{Re}\left\{\sum_{p=-\infty}^{\infty}\tilde{E}_{p3}\exp\left[i\left(-p\frac{\pi}{2}-\frac{\pi}{4}\right)\right] I(kr,p)\right\} \text{ where}$$

$$I(kr,p) = \int_0^\pi \exp[ikr(1-\cos\theta) + ip\theta](1+\cos\theta)\, d\theta$$

p is some fixed integer, and kr = kR is on our integration surface, so it is arbitrarily large. We evaluate the asymptotic expression for this integral by the method of steepest descent. The following exposition is more or less self-contained; for a fuller treatment, see Arfken,[e] whose notation we follow.

We have an integral of the form:

$$I(s) = \int_C g(z)\, e^{s\, f(z)}\, dz$$

where z is an extension of θ into the complex plane. We write z = x + iy.
C is the (open) contour from 0 to π along the x axis.

$$g = e^{ipz}\,(1+\cos z), \qquad s = kr, \qquad \text{and } f = i\,(1-\cos z) = u + iv.$$

To find the steepest descent, we must deform the contour so that it goes through any saddle points along level curves of v. The Cauchy-Riemann conditions assure us that a level curve of v is parallel to the gradient of u at that point, so this is the path of steepest descent. Since s is large, the whole contribution to the integral comes from the region around the saddle point.

[e] G. Arfken, *Mathematical Methods for Physicists*, 3rd edition, Academic Press, Orlando, Section 7.4

$$f = -\sin x \sinh y + i(1 - \cos x \cosh y) = u + iv$$

$$\frac{\partial u}{\partial x} = -\cos x \sinh y = 0$$

$$\frac{\partial u}{\partial y} = -\sin x \cosh y = 0$$

We have two saddle points: (0, 0) and (π,0). For the first, v is constant along y = $\cosh^{-1}$ (sec x), and for the second, along y = $\cosh^{-1}$ (-sec x). So we deform the contour along C to C_1, which goes from 0 to $\pi/2 + i\infty$, plus C_2, which comes back from $\pi/2 + i\infty$ to π.

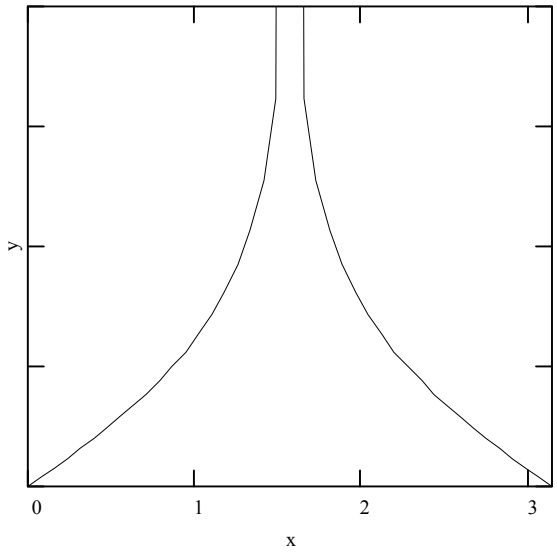

Figure A7. Saddle Points for the Solution

The value of the integral is unchanged under this deformation because there are no singular points between the two contours. As $z \to \pi/2 + i\infty$, $u \to -\infty$, so $e^{sf} \to 0$. A test of the second derivative at both saddle points shows that both points are maxima along the indicated contour.

$$f(z) = f(z_0) + \tfrac{1}{2} f''(z_0) (z - z_0)^2 + \ldots$$

Define t so that $\tfrac{1}{2} f''(z_0) (z - z_0)^2 = -t^2 / 2s$. Also, $z - z_0 = \delta e^{i\gamma}$, At $z_0 = (0, 0)$, $\gamma = \pi/4$ and at $z_0 = (\pi, 0)$, $\gamma = 3\pi/4$. $t^2 = sf''(z_0) \delta^2 e^{2i\gamma}$. We choose v constant along our contour, so Im $(f(z) - f(z_0)) = 0$ and $\tfrac{1}{2} f''(z_0) (z - z_0)^2$ is real. $t = \pm\delta |sf''(z_0)|^{1/2}$, where the straight brackets denote complex amplitude.

$$I(s) = g(z_0)\exp(sf(z_0))\int_{-\infty}^{\infty}\exp\left(-\frac{t^2}{2}\right)\frac{dz}{dt}dt$$

$$\frac{dz}{dt} = \frac{1}{\frac{dt}{dz}} = \frac{1}{\frac{dt}{d\delta}\frac{d\delta}{dz}} = \frac{1}{\left|s f''(z_0)\right|^{1/2} e^{-i\gamma}}$$

$$I(s) = \frac{\sqrt{2\pi}g(z_0)\exp(s f(z_0))\, e^{i\gamma}}{\left|s f''(z_0)\right|^{1/2}}$$

We must add the expressions for both points:

$$I(s) = \frac{\sqrt{2\pi}\, e^{ip0}(1+\cos 0)\, e^{kRi(1-\cos 0)}\, e^{i\pi/4}}{\left|kRi\cos 0\right|^{1/2}} + \frac{\sqrt{2\pi}\, e^{ip\pi}(1+\cos\pi)\, e^{kRi(1-\cos\pi)} e^{i3\pi/4}}{\left|kRi\cos\pi\right|^{1/2}} = 2\sqrt{\frac{2\pi}{kR}}\, e^{i\pi/4}$$

Then the second term gives:

$$-2\varepsilon_0 \ell R \frac{E_1}{2}\sqrt{\frac{2}{\pi kR}}\,\mathrm{Re}\left\{\sum_{p=-\infty}^{\infty}\widetilde{E}_{p3}\exp\left[i\left(-p\frac{\pi}{2}-\frac{\pi}{4}\right)\right]2\sqrt{\frac{2\pi}{kR}}\, e^{i\pi/4}\right\}$$

$$= -4\varepsilon_0 \ell E_1 \tfrac{1}{k}\,\mathrm{Re}\left(\sum_{p=-\infty}^{\infty}\widetilde{E}_{p3}\, e^{-i\,p\,\pi/2}\right)$$

This is the same for each wire, so summing over the wires gives a simple multiplication by N. Recall $\ell = Nd$.

Term 2:

$$-4\varepsilon_0 E_1 \tfrac{1}{k} N^2 d\sum_{p=-\infty}^{\infty}\mathrm{Re}\left(\widetilde{E}_{p3}(-i)^p\right)$$

The reflected waves produce an interference pattern with each other, so we must sum the fields before we square E_R, and the sin Nα / sin α factor appears.

Term 1:

$$-2\varepsilon_0 \ell R\int_0^{\pi} E_R{}^2\cos\theta d\theta$$

$$= -2\varepsilon_0 \ell R\frac{2}{\pi kR}\int_0^{\pi}\left(\frac{\sin N\alpha}{\sin\alpha}\right)^2\left\{\sum_{p=-\infty}^{\infty}\left[\begin{array}{l}\mathrm{Re}\,\widetilde{E}_{p3}\cos\left(kR - p\frac{\pi}{2} - \frac{\pi}{4} + p\theta - \omega t\right)\\ -\mathrm{Im}\,\widetilde{E}_{p3}\sin\left(kR - p\frac{\pi}{2} - \frac{\pi}{4} + p\theta - \omega t\right)\end{array}\right]\right\}^2\cos\theta d\theta$$

Averaging over time as before gives:

$$\frac{-4\varepsilon_0 \ell}{\pi k}\int_0^{\pi}\left(\frac{\sin N\alpha}{\sin\alpha}\right)^2\cos\theta\,d\theta \sum_{p=-\infty}^{\infty}\sum_{q=-\infty}^{\infty}\left[\begin{array}{l}\frac{1}{2}(\mathrm{Re}\,\tilde{E}_{p3}\,\mathrm{Re}\,\tilde{E}_{q3}+\mathrm{Im}\,\tilde{E}_{p3}\,\mathrm{Im}\,\tilde{E}_{q3})\cos((p-q)(\theta-\frac{\pi}{2}))\\ +\frac{1}{2}(\mathrm{Re}\,\tilde{E}_{p3}\,\mathrm{Im}\,\tilde{E}_{q3}-\mathrm{Im}\,\tilde{E}_{p3}\,\mathrm{Re}\,\tilde{E}_{q3})\sin((p-q)(\theta-\frac{\pi}{2}))\end{array}\right]$$

By the symmetry of the reflection $\theta \to \pi - \theta$,

$$\mathrm{Term1} = -4\frac{\varepsilon_0 \ell}{\pi k}\int_0^{\pi/2}\sum_{p=-\infty}^{\infty}\sum_{q=-\infty}^{\infty}\left[\begin{array}{l}\left(\mathrm{Re}\,\tilde{E}_{p3}\,\mathrm{Im}\,\tilde{E}_{q3}-\mathrm{Im}\,\tilde{E}_{p3}\,\mathrm{Re}\,\tilde{E}_{q3}\right)\\ \sin((p-q)(\theta-\pi/2))\left(\frac{\sin N\alpha}{\sin\alpha}\right)^2\end{array}\right]\cos\theta\,d\theta$$

Consider the quantity $\frac{kd}{2\pi N}\left(\frac{\sin N\alpha}{\sin\alpha}\right)^2\cos\theta$. (Remember that $\alpha = kd\sin\theta / 2$.) Figure A8 shows $\left(\frac{\sin N\alpha}{\sin\alpha}\right)^2$ versus θ for N = 5 and for N = 10. kd = 3.

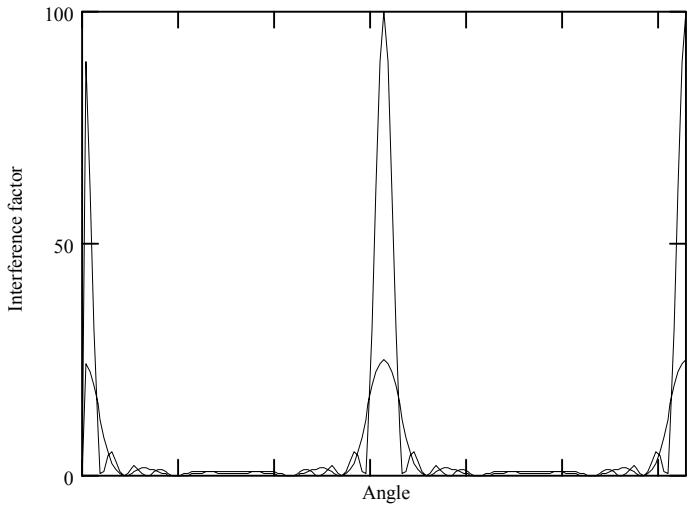

Figure A8. Behavior of $(\sin N\alpha/\sin\alpha)^2$

It is seen that the function is appreciable only when $\alpha \approx m\pi$, m = 0, ±1, ±2 … Also, as N increases, the function becomes taller and narrower.

$$A = \frac{kd}{2\pi N}\int_{\sin^{-1}\lambda(m-1/2)/d}^{\sin^{-1}\lambda(m+1/2)/d}\left(\frac{\sin N\alpha}{\sin\alpha}\right)^2\cos\theta\,d\theta$$

is the area under the curve contained in one lobe. With a change of variables,

$$A = \frac{1}{\pi N}\int_{\pi(m-1/2)}^{\pi(m+1/2)}\left(\frac{\sin N\alpha}{\sin\alpha}\right)^2 d\alpha = \frac{1}{\pi N}\int_{-\pi/2}^{\pi/2}\left(\frac{\sin N\alpha}{\sin\alpha}\right)^2 d\alpha = 1,$$ [f]

so this combination of factors is a Dirac delta function as $N \to \infty$. We must sum over the separate lobes:

$$\text{Term } 1 = \frac{-4\varepsilon_0 Nd}{\pi k}\frac{2\pi N}{kd}\int_0^{\pi/2}\sum_{m=0}^{\|d/\lambda\|}\delta(\theta - \sin^{-1}\tfrac{m\lambda}{d})\times$$
$$\sum_{p=-\infty}^{\infty}\sum_{q=-\infty}^{\infty}(\mathrm{Re}\,\tilde{E}_{p3}\,\mathrm{Im}\,\tilde{E}_{q3} - \mathrm{Im}\,\tilde{E}_{p3}\,\mathrm{Re}\,\tilde{E}_{q3})\sin((p-q)(\theta-\tfrac{\pi}{2}))d\theta$$

$\| d / \lambda \|$ is the greatest integer less than or equal to d / λ.

$$\frac{dp_x}{dt}(a,d,\lambda) = \frac{-8\varepsilon_0 N^2}{k^2}\sum_{p,q}\mathrm{Im}(\tilde{E}^*_{p3}\tilde{E}_{q3})\sum_{m=0}^{\|d/\lambda\|}\sin((p-q)(\sin^{-1}\tfrac{m\lambda}{d} - \tfrac{\pi}{2}))$$
$$-4\varepsilon_0 E_1 \tfrac{1}{k} N^2 d\sum_{p=-\infty}^{\infty}\mathrm{Re}\left(\tilde{E}_{p3}(-i)^p\right)$$

As a demonstration that the treatment so far has been correct, we calculate the quantity:

$$R(\lambda,a,d) = \frac{\frac{1}{2}\frac{dp_x}{dt}}{A\,\frac{1}{2}\varepsilon_0 E_1^{\,2}}$$

The denominator is the total momentum flowing across an area the size of the sail from that portion of the solar spectrum at wavelength λ. The quantity of interest is the thrust to mass, or acceleration:

$$T_m(a,d) = \frac{\frac{1}{c}\int_0^{\infty} 2R(\lambda,a,d)\,s(\lambda)\,d\lambda}{2\rho\pi a^2/d}$$

where c is the speed of light, ρ is the density of aluminum (2.7 gm / cm^3), and s is the solar irradiance at 1 AU (in W/m^2 wavelength interval). The mass of one wire is $\rho\pi a^2\ell = \rho\pi a^2 Nd$, and there are 2N of them, so $m/A = 2\rho\pi a^2/d$.

Note added: T_m was solved numerically and plotted earlier as Figure 8. Maximum accelerations of 0.54 m/s^2 were obtained for a grid of aluminum wires and 17 m/s^2 for a grid of doped carbon nanotubes, as compared to the order of magnitude higher numbers obtained by extending microwave reflection theory.

[f] I. S. Gradshteyn & I. M. Ryzhik, *Table of Integrals, Series and Products*, Academic Press, 1980, formula 3.624.6